

MM Science Journal | www.mmscience.eu

ISSN 1803-1269 (Print) | ISSN 1805-0476 (On-line)

Special Issue | HSM 2025

18th International Conference on High Speed Machining October 15-16, 2025, Metz, France

DOI: 10.17973/MMSJ.2025_11_2025144



HSM2025-44840

NUMERICAL INVESTIGATION OF TOOL WEAR EFFECTS ON PROCESS QUANTITIES DURING TURNING OF AISI 4140

A. Kenfack^{1,2*}, L. Langenhorst^{1,2}, J. Solter^{1,2}, A. Fischer^{1,3}, B. Karpuschewski^{1,2}

¹University of Bremen, MAPEX Center for Materials and Processes, Badgasteiner Str. 1, 28359 Bremen, Germany

²Leibniz Institute for Materials Engineering IWT, Badgasteiner Str. 3, 28359 Bremen, Germany

³University of Bremen, Bremen Institute for Metrology, Automation and Quality Science, Linzer Str. 13, 28359

Bremen, Germany

*Corresponding author; e-mail: kenfack@iwt-bremen.de

Abstract

To manufacture components with a certain pre-defined surface integrity, it is important to understand how tool wear affects the machined workpiece. In this work, an approach is proposed to simulate the effect of tool wear based on measured geometries of worn turning tools on process forces for different feeds. In orthogonal cutting simulations utilizing the Coupled Eulerian-Lagrangian (CEL) finite element method, forces are simulated and compared to cutting experiments. As input for the simulations, 3D tool geometries are decomposed into several 2D profiles. The results show a reasonable agreement of simulation and experiment laying the foundation for further analysis of surface integrity effects.

Keywords:

Orthogonal cutting, Finite element method (FEM), Modelling, Process forces, Tool wear

1 INTRODUCTION AND STATE OF THE ART

With the drive towards more sustainable manufacturing processes, dry machining is becoming more adopted. Due to the absence of metal working fluids, the environmental, safety and health hazards associated with their usage are considerably avoided. As a consequence, problems might arise associated with the unlubricated friction leading to high mechanical loads and high temperatures. These affect the cutting edge region of the tool and facilitate the abrasive wear at the flank face of the tool thus affecting its performance and the machined surface [Sun 2013]. By developing two techniques designed to measure the surface temperature of machined components, O'Sullivan and Cotterell not only showed that the machined surface temperature increases with increasing flank wear but also that by increasing the cutting speed, the temperature decreases [O'Sullivan 2001]. The increase in cutting speed caused a faster removal of the chips formed and consequently reduced the time for the heat conduction to occur. However, in some cases an increase in cutting speed leads to an increase in the cutting power und subsequently to an increase in the amount of heat generated [Tönshoff 2000]. Because tool wear affects process quantities such as process forces and heat fluxes differently depending on the tool geometry, workpiece material and cutting conditions, it is important to understand how different tool geometry affects these quantities.

Tool wear does not only have a significant influence on surface roughness and process forces, but also on the tool service life, process energy consumption, residual stresses and strains induced in the workpiece surface layer.

Depending on the region where the tool wear is located, it can be subdivided into three main modes, namely: flank wear, crater wear and notch wear [Agapiou 2013]. Studies have shown that in comparison to other tool wear, flank wear affects the dimensional accuracy and reliability of the machining process [Astakhov 2004]. Therefore, quantitatively determining the changes in the process forces during the machining process greatly contributes in better understanding the effects of tool wear on the machined component and energy consumption [Liu 2016]. During machining of 16MnCrS5, Meyer et al. compared

During machining of 16MnCrS5, Meyer et al. compared tools with smaller and larger nose radii and showed that for the same cutting time, tools with smaller nose radii not only led to a reduction in the process forces but also greatly reduced the service life of tools [Meyer 2012]. This was explained by the reduction in the contact between the tool and the workpiece.

Besides experimental studies, many works have also been published based on numerical simulations and using commercial finite element (FE) software like DEFORM and ABAQUS to predict the influence of tool wear on the cutting and feed forces, cutting temperature, and the residual stresses induced [Özel 2009, Munoz-Sanchez 2011, Ducobu 2015]. Utilizing the updated Lagrangian (UL) and the arbitrary Lagrangian-Eulerian (ALE) method, Özel investigated the effects of flank wear on the process forces and temperatures obtained with these approaches. The results showed the UL method to be more accurate and that the feed forces are more sensitive to flank wear with the discrepancy between experimental and simulated values being smaller than with new tools [Özel 2009]. A similar

tendency was also observed by Equeter et al. after performing a chip formation simulation utilizing the coupled Eulerian-Lagrangian (CEL) method [Equeter 2018]. The commercial software Abaqus/Explicit enables the execution of both 3D and orthogonal cutting (2D) simulations using the Eulerian, Lagrangian, ALE and CEL approaches. Although the CEL method has a higher computational cost when compared to the other methods, its ease of setup and capability to model large deformations during the cutting simulation is very advantageous and does not require several attempts to find the correct chip geometry [Aridhi 2022]. It has also been successfully implemented in orthogonal cutting simulations [Munoz-Sanchez 2011, Ducobu 2017, Aridhi 2022], where the workpiece and the cutting tool are modelled in the Eulerian and Lagrangian domain respectively.

While several studies have investigated the effects of tool wear on process forces during orthogonal cutting, few have actually analyzed how a whole new tool geometry generated during the turning process affects these quantities. This paper uses the CEL approach to help better understand the influence of different tool geometries resulting from wear effects on these quantities by discretizing both new and worn 3D tool geometries into sections to build 2D tools with different local uncut chip thicknesses for orthogonal cutting simulations.

2 OBJECTIVE AND PROCEDURE

The main objective of this work is to investigate the effects of different tool geometries as a result of tool wear on process forces by utilizing 2D chip formation simulations based on the CEL approach. A basic model is to be initially validated by comparing the simulated forces with the experimental and simulated ones presented in [Meurer 2022]. Following the validation of the model, it will be utilized to perform orthogonal cutting simulations with 2D sections measured at new and worn turning inserts to capture the change of the tool geometry more comprehensibly. To discretize the whole tool geometry into several 2D sections, an approach similar to that published in [Clavier 2024] will be used. Fig. 1 summarizes in detail the analysis steps of this work.

All turning experiments were carried out on a machine tool of type DMG Mori NEF400 equipped with a three jaw chuck. Mounted on the machine tool to measure the forces is a three-component dynamometer of type KISTLER 9121 with a corresponding charge amplifier of type KISTLER 5019 A (Fig. 2). All three-force components (cutting force F_c , feed force F_f , and passive force F_p) were recorded at a sampling rate of 1000 Hz. For subsequent evaluations, the average value of the last second within the force signals were used, as these forces result from the tool wear state measured after the process. In case of unworn tools, the last second before a cutting length of 3 m has been reached was used for force evaluation.

The workpiece material used to conduct these turning experiments was quenched and tempered AISI 4140 steel (Fig. 2). It was heated in a vacuum oven 10 K/min to a temperature of 850 °C. The heating was followed by a holding period of 2 hours and then quenched in oil to 60 °C before tempering at 400 °C for 4 hours. Following these steps, the workpiece exhibited a hardness of 47 HRC. Cutting inserts CCMW09T304 from Sandvik Coromant used in these experiments are made of coated tungsten carbide. The inserts have a rake angle γ = 0°, a clearance angle γ = 7° and a nose radius γ = 0.4 mm. A tool holder

SCLCL2020K09 also from Sandvik Coromant built an inclination angle λ = 0 ° and a cutting edge angle κ = 95 °.

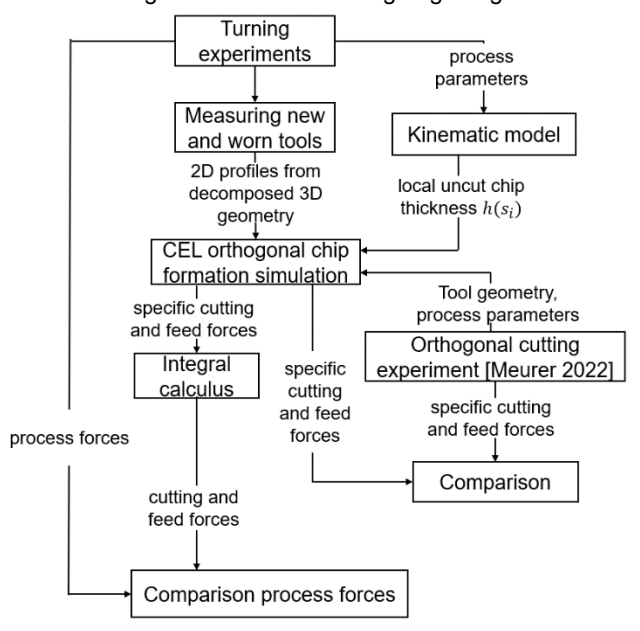


Fig. 1: Procedure for the investigation of the effects of different tool wear states on process forces.

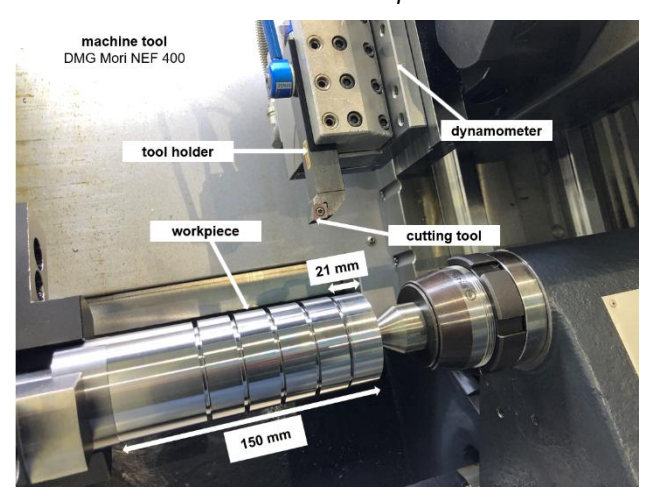


Fig. 2: Experimental setup.

Some inserts had previously been utilized in a controlled turning process with the same machining parameters as in the later experiments involving the same workpiece in order to generate specific initial wear states. To realize different wear states, these tools were inserted and required to complete different cutting lengths $l_{\rm c}$. The experiments were carried out with the machining parameters presented in Tab. 1.

Tab. 1: Cutting conditions.

Cutting speed v _c [m/min]	200
Feed rate f [mm/rev]	0.1 / 0.2
Depth of cut a _p [mm]	0.75

Measurements of 3D geometries of each insert before and after the experiments (Fig. 3) were realized using the Alicona InfiniteFocus G5 device from Bruker. To maintain the inserts in the same fixed position during the measuring process and therefore minimize possible discrepancies, the inserts were fixed on a bore rod A20S-SCLCL09 from Sandvik Coromant and inserted between the jaw chuck of

the device. The placement of the bore rod remained unchanged and the measurement coordinates of the Alicona software were saved to ensure consistency.

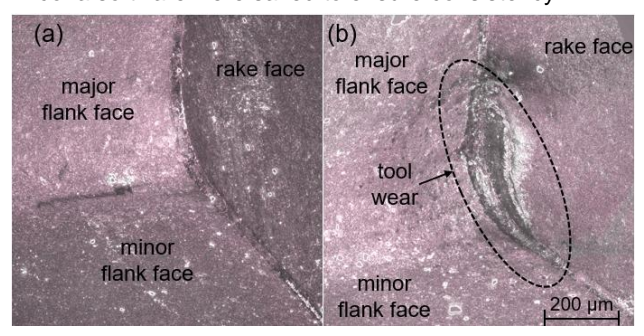


Fig. 3: 3D topography of (a) new tool and (b) worn tool.

3 NUMERICAL MODEL

3.1 Model development/Modelling approach

Decomposing the 3D tool geometry into 2D sections

After opening the 3D geometry of a new tool in the Alicona user interface, the X (red) and Y (green) - axis of the coordinate system were placed alongside and tangential to the main cutting edge of the 3D geometry respectively (Fig. 4). This enabled the rake face of the insert geometry to lie perfectly on the XY-plane of the coordinate system. With the Y-axis of the coordinate system corresponding to a depth of cut $a_p = 0$ mm, the cutting edge was decomposed into five different 2D sections. The profile data of each section (consisting of the rake face, the clearance face and the cutting edge) was then extracted and the 2D tool geometries were generated using Autodesk Inventor and later imported in STEP file format in Abagus/Explicit, Since all the 3D geometries were generated using the same measuring coordinates, the exact same coordinate system that had been used to determine $a_D = 0$ mm for the new tool, was used in decomposing each section of the worn tools. By modifying the analytical model to determine the uncut chip thickness during face milling developed by Langenhorst et al. [Langenhorst 2019], h(s₁₋₅) could be calculated with each section being perpendicular to the interior (right) side of the uncut chip geometry (Fig. 5). Since both the rake and the inclination angle are equal to zero, orthogonal cutting conditions are assumed for these calculations with no chip flow in the out of plane direction. Also, as a first order approximation, changes in the uncut chip thicknesses due to tool wear were not considered. Fig. 5 also shows the specific forces acting on the tool during the turning process, in cutting direction (Fc), feed direction (F_f), and perpendicular to both directions (F_p). By means of the specific cutting normal force FcN resulting from 2D orthogonal cutting simulations, the specific feed and passive forces can be calculated based on vector calculus and considering the horizontal angle, for example θ_{s3} for section s₃ in Fig. 5.

Model geometry

The Eulerian domain, which includes the workpiece and the void region, was meshed with EC3D8RT thermally coupled elements types with reduced integration. This element type is not implemented in Abaqus as two-dimensional elements. For this reason, the width of cut was made up of one element and chosen to be significantly smaller (2 μ m) than the length and height of the Eulerian domain (Fig. 6).

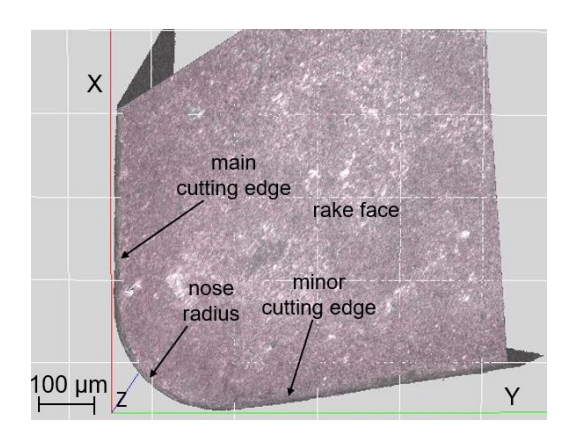


Fig. 4: Generated 3D geometry of a new tool and the coordinate system used to decompose into 2D profiles.

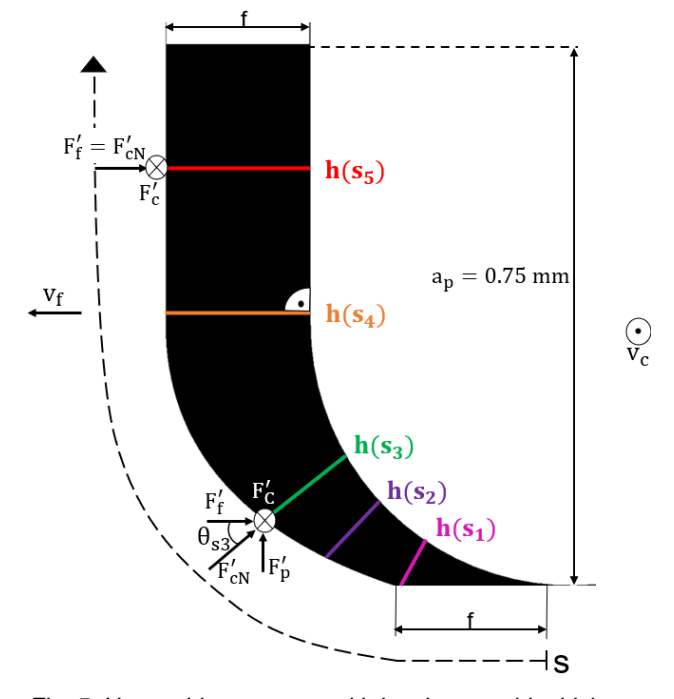


Fig. 5: Uncut chip geometry with local uncut chip thickness and the specific forces acting on the cutting tool in dependence of the distance along the cutting edge s of an unworn tool.

This enabled the model to be considered as a 2D plane strain model. While the finer region of the Eulerian domain contained 5 μm x 5 μm elements, the rest of the domain was made up of 5 μm x 10 μm elements. The tool was defined as a rigid body and meshed with C3D8T also thermally coupled element type. Similar to the Eulerian domain, the tool had a thickness of 2 μm with element sizes ranging from 5 - 25 μm .

All the nodes of the Eulerian domain were assigned a zero-velocity in the out-of-plane direction ($v_z=0$) to avoid material flow. A zero-velocity in the y-direction was given to the nodes located at the bottom of the domain. This assured that there was no material flow downwards out of the domain. A reference point was defined on the tool to apply the cutting speed value. Both domains were allocated an initial temperature of 298 K which corresponds to the room temperature during the turning experiments. To enable heat transfer at the tool-workpiece interface, a pressure dependent gap heat conductance was applied. The workpiece material was assigned an inelastic heat fraction (Taylor-Quinney factor) of 0.9.

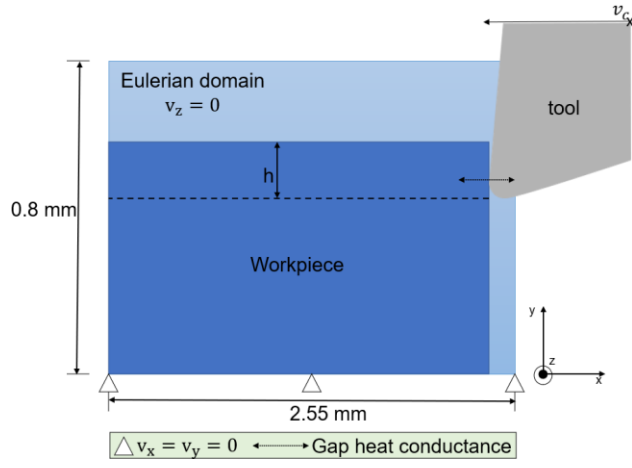


Fig. 6: Chip formation model using the CEL method.

Material

To describe the thermomechanical behavior of AISI 4140 QT, the Johnson-Cook (JC) model was used. It considers isotropic strain hardening, strain rate hardening and thermal softening [Johnson 1985].

$$\bar{\sigma} = (A + B\bar{\varepsilon}^n) \left[1 + C \ln \left(\frac{\dot{\varepsilon}}{\dot{\varepsilon}_0} \right) \right] \left[1 - \left(\frac{T - T_r}{T_m - T_r} \right)^m \right] \tag{1}$$

In Equation 1, A represents the yield stress at room temperature T_r, T_m is the melting point temperature and $\overline{\epsilon}$ is the equivalent plastic strain. $\dot{\bar{\epsilon}}$ and $\dot{\bar{\epsilon}}_0$ are the equivalent and reference plastic strain rate respectively. B, C, n and m are model coefficients. The JC material parameters for AISI 4140 QT and the material parameters for AISI 4140 QT and WC-Co are listed in Tab. 2. At the chip-tool and tool-machined surface interfaces, the friction model significantly affects the chip flow and process quantities. Thus, using a suitable friction model greatly improves the simulation results. In this work, a constant friction coefficient $\mu=0.095$ for the cutting speed $v_c=100$ m/min and $\mu=0.07$ for the cutting speed $v_c=200$ m/min were used [Buchkremer 2017].

Tab. 2: Material parameters of the chip formation model [Meurer 2020, Meurer 2022].

JC constitutive model		A (MPa)	1450	
		B (MPa)	910	
		С	0.034	
		m	0.328	
		n	0.45	
		$\dot{\bar{\epsilon}}_0$	0.001	
		$T_{r}(K)$	298	
		T _m (K)	1809	
		AISI 4140	Carbide	
Young's Modulus, E (MPa)		204223	60000	
Poisson's ratio, v (-)		0.3	0.22	
Density, ρ (kg/m³)		7619	15000	
Conductivity, k (W/mK)		42.6	66.3	
Therm. Expansion, α (K ⁻¹)		12.3e ⁻⁶	4.7e ⁻⁶	
Specific heat capacity c _p (J/kgK)				
AISI 4140	2·10 ⁻⁴ ·T ² + 477.04 - 0.0654·T			
Carbide	250			

3.2 Model validation and mass scaling

To validate this model, orthogonal cutting simulations similar to those in Meurer et al. [Meurer 2022] were performed. With the exception of the software and the chip formation model used, the simulation parameters were the same. Fig. 7a shows the results obtained for an uncut chip thickness h = 0.1 mm and at a cutting velocity v_c = 100 m/min. Even though both simulated cutting forces are relatively equal, there is still a maximum average error of 20% when comparing these results to the experimental cutting forces published in [Meurer 2022]. While the deviation between experiment and simulation from Meurer et al. is also evident for the feed force, the change in chip formation model also results in deviations. In order to reduce the computational cost associated with the CEL method, two strategies have been developed namely, time scaling and mass scaling [Hammelmüller 2015]. For simulations involving chip formation, mass scaling has been shown to being the only useful strategy due to the wide range of strain rates associated with chip formation. The mass scaling strategy comprises of respectively substituting the density p and the specific heat capacity cp by a fictitious density ρ^* and specific heat capacity c_p (Equations 2 and 3), respectively.

$$\rho^* = k_m \cdot \rho \tag{2}$$

$$c_p^* = k_m^{-1} \cdot c_p \tag{3}$$

 k_m represents the factor by which the critical time increment will be increased and thus reducing the calculation time by $\sqrt{k_m}$. Fig. 7b shows that even with k_m = 1000, the effects on the process forces are very minimal when compared to factors of 1 and 100. For this reason, a factor of 1000 was chosen for the subsequent simulations.

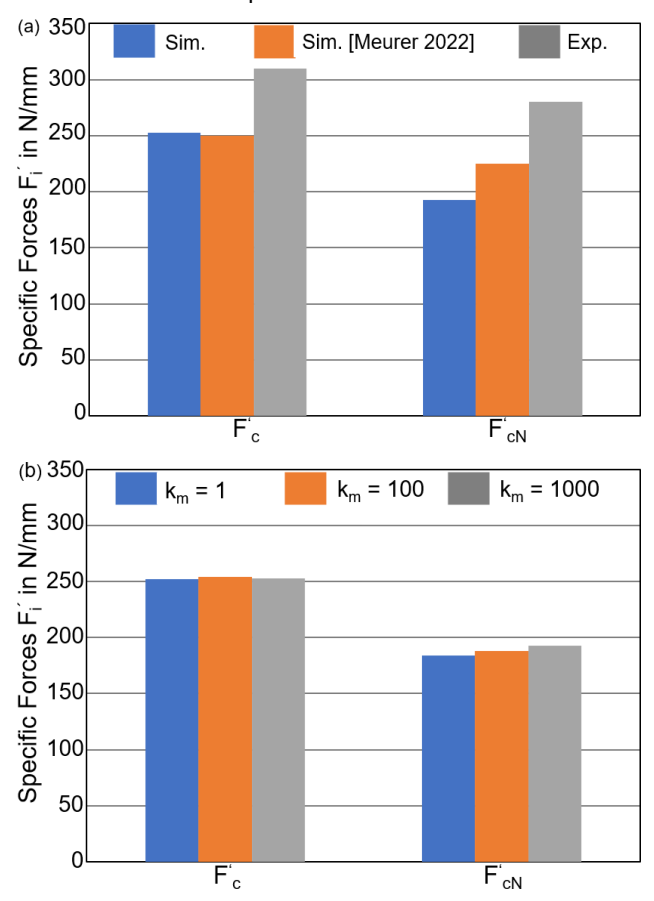
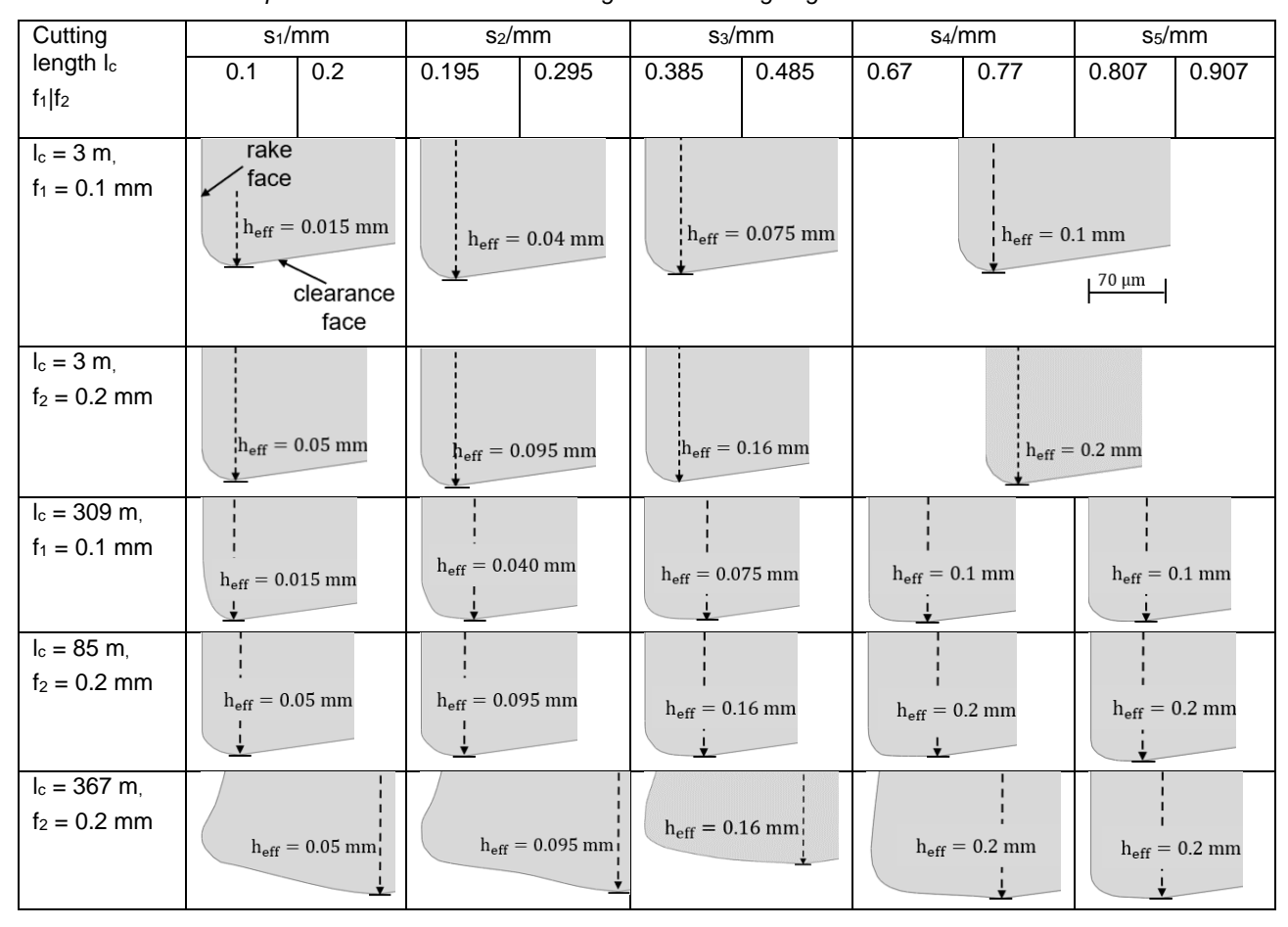


Fig. 7: a) Simulated and measured specific cutting and cutting normal forces and b) influence of different mass scaling factors on these specific forces.

Tab. 3: 2D profiles and effective uncut chip thickness heff of each section used in the chip formation simulations in dependence with the distance along the tool cutting edge s and the feed rate f.



4 RESULTS AND DISCUSSION

After the completion of the turning experiments, the total cutting length of each tool was calculated and the different 2D tool profiles were generated from both new and worn 3D tool geometries as previously mentioned (Tab. 3). Tab. 3 also shows the effective local uncut chip thicknesses, $h_{\text{eff}}(s_i)$ of the different 2D profiles used in this work. These values were calculated by modifying the analytical model developed by [Langenhorst 2019] (see section 3.1). Even though the wear state of each tool was not explicitly considered when determining each value of $h_{\text{eff}}(s_i)$, it was integrated in the simulations by making sure the distance between the lowest point along the clearance face region of the tool and the surface of the uncut workpiece corresponded to each value of $h_{\text{eff}}(s_i)$.

The average specific cutting (F_c) and feed force (F_f) obtained after the simulations with the different 2D profiles and the local uncut chip thicknesses (Tab. 3) were then plotted against the distance travelled along the cutting edge s (Figs. 8 and 9). The data of each curve were then fitted with appropriate functions.

In the case of the specific cutting forces (Fig. 8), a saturation function was chosen to fit the data of each tool because with increasing distance along the cutting edge (s_{1-3} in Tab. 3), the differences in both the tool geometries and the effective uncut chip thicknesses increase. This leads to a continuous increase in F_c . However, F_c remains approximately constant from s_4 upwards because even though s increases, $h_{\text{eff}}(s_{4-5})$ remain constant and the differences in

the tools' geometries reduces. This is particularly noticeable for the tools with $l_{\rm c}=367$ m and $l_{\rm c}=85$ m. The tool with $l_{\rm c}=367$ m experiences significantly higher specific cutting forces for the same distance along the cutting edge and the same $h_{\rm eff}(s_i)$ than that with $l_{\rm c}=85$ m due to the difference in their geometries. The difference in the $F_{\rm c}$ ' experienced by both tools reduces and are close in value once the difference in their tool geometries also reduces (s_5) . In the case of the unworn tools, the values of the specific force mainly depend on $h_{\rm eff}(s_i)$ since the tool geometries are roughly the same with increasing value of s.

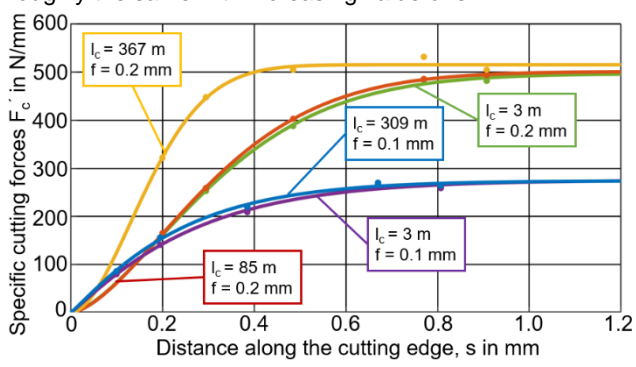


Fig. 8: Simulated specific cutting forces for different cutting lengths along the cutting edge with curve progressions.

Moreover, as seen in Fig. 9, two different functions were used to fit and describe the specific feed forces (Fig. 9). The same saturation function used for F_{c} was chosen to fit the data of the unworn tools because of the small difference in the F_{f} values once the maximum specific feed force is reached (s₄₋₅). To describe and fit the data of the worn tools,

a mixture of a Gaussian and an exponential function was selected. The Gaussian part of this function describes the fast increase in the values of $F_{\rm f}$. This shows that the specific feed force is more sensitive to changes in tool geometry than changes in the effective uncut chip thickness. This observation can be confirmed by comparing the significant differences in the values of $F_{\rm f}$ between $s_{1\text{-}3}$ for the tool with $l_c=367$ m with the tool with $l_c=85$ m. These differences reduce with increasing s and effective uncut chip thickness (heff(s_3-4)). This results from both smaller differences in the tools' geometries and smaller increase in $h_{\rm eff}(s_i)$ (heff(s_{1\text{-}2})=0.09 mm and $h_{\rm eff}(s_{3\text{-}4})=0.04$ mm).

To describe the data of the worn tools after F_f' reached its maximum value, the exponential part of the function was executed. This function captures the gradual decrease in the values of F_f' resulting from the small changes in the geometries of the tools at constant $h_{\text{eff}}(s_{4-5})$. The function makes sure that once all the tools used at the same feed rate have almost the same geometries and $h_{\text{eff}}(s_i)$ (unworn part along the cutting edge), the specific feed forces will approximately be equal.

Furthermore, the dark brown curve with its secondary y-axis in Fig. 9 represents the cutting normal force (F_{cN}) of the tool with $I_c=367\,$ m. To fit these data, a modified sigmoid function was used. This function captures the initial increase in the value of F_{cN} along the cutting edge of the tool (s_{1-3}) resulting from the vector addition of F_f and F_p (Fig. 5, $h(s_{1-3})$). Once $F_p=0$, the cutting normal force is equal to the feed force component (Fig. 5, $h(s_{4-5})$) and both curves (F_{cN} and F_f) progress almost identically as the values of F_{cN} also decrease due to smaller discrepancies between the tool geometries.

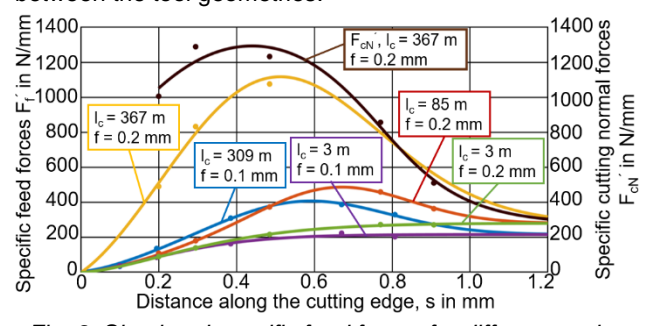


Fig. 9: Simulated specific feed forces for different cutting lengths and specific cutting normal force along the cutting edge with curve progressions.

By using the trapezoidal numerical integration method along the tool's cutting edge s (Equations. 4 and 5), the total cutting and total feed force of each cutting tool incorporating their individual wear state could be calculated (Fig. 10).

$$F_{c} = \int_{0}^{s_{5}} F_{c}' ds \tag{4}$$

$$F_f = \int_0^{s_5} F_f' ds$$
 (5)

In equations 4 and 5, s_5 = 1.057 mm and 1.157 mm for the tools used at feed rates of 0.1 mm and 0.2 mm, respectively.

Fig. 10 shows relatively good agreement between the simulated and the experimental cutting forces with a maximum difference of 14%. The discrepancies increase when comparing the simulated and the experimental feed forces (maximum difference of 20%) of the unworn tools. These results mirror the results displayed in Fig.7(a) where the simulation underestimated the experimental value. Fig. 10 also shows a larger percentage increase in the simulated feed forces results from unworn tool to worn tools at the same feed rates (increases of 63% and 239% for

f = 0.1 mm and f = 0.2 mm, respectively) than in the simulated cutting forces (increases of 3% and 23% for f = 0.1 mm and f = 0.2 mm, respectively). This confirms the observation that the feed forces are more sensitive to changes in geometry with a maximum difference of 23%. This sensitivity to geometry changes is supposedly due to an increase in the contact area between the worn tool and the machined surface. This can be seen when comparing both the simulated and experimental feed forces of the tool with a cutting length of 367 m with those with a cutting length of 85 m. This is the case even though both tools were used at the same feed rate and have the same effective uncut chip thicknesses. Another reason for this difference in the feed forces could be the added ploughing effect taking place due to the smaller uncut chip thicknesses during the simulations with the 2D profiles of the tool with $I_c = 367 \text{ m} (Tab. 3).$

It should be noted that only in the case of the tool with a cutting length of 367 m, the experimental value represents the average of the minimum and maximum values recorded during the experiment (Fig. 10). This was because the recorded force signals were still increasing due to the continuously increasing tool wear state before the experiment was stopped.

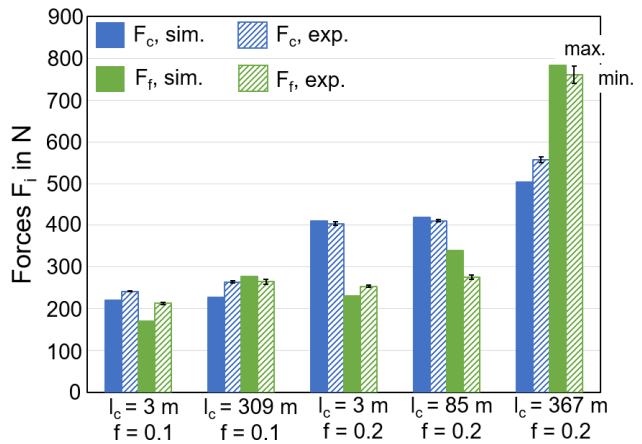


Fig 10: Calculated and measured cutting and feed forces.

5 SUMMARY AND OUTLOOK

In this study, the effects of different tool geometries as a result of tool wear are investigated by developing a 2D CEL chip formation model. The experimentally worn inserts were measured and discretized into several 2D profiles to be used in the chip formation simulation. By utilizing this developed model, the specific cutting and feed forces with varying local uncut chip thickness were calculated. The results showed that even though changes in the geometries of the tools lead to an increase in the specific cutting forces, the specific feed forces were more sensitive to these changes. It could also be observed that the changes in the geometry of a tool have a higher influence on these specific forces than an increase in the effective uncut chip thickness. Based on these results, the cutting and feed forces acting on each tool were determined through numerical integration. The results further confirmed the initial observation that the feed forces were more sensitive to changes in tool geometry as the discrepancies between simulated and experimental results reduced. This was also observed when comparing the percentage increase in the values of the feed forces between the unworn and worn tools at the same feed rates.

Future studies will focus on investigating how different tool geometries due to wear affect the residual stresses induced beneath the machined surface. To achieve this, a Lagrangian model with a coupled temperature-displacement step will be developed to simultaneously simulate the redistribution of the stresses within the machined workpiece and its cooling. The simulated induced residual stresses will be compared with experimental results to validate the model. Finally, it is expected that by building correlations between process quantities, e.g. forces and heat fluxes, and the internal material loads, e.g. strains and temperatures, the effects of tool wear during turning on surface integrity will be better understood.

6 ACKNOWLEDGMENTS

The authors thank the German Research Foundation (DFG) for funding this work within the SPP 2402 – project no. 521384759 and the transregional Collaborative Research Centre SFB/TRR 136 – project no. 223500200. The authors also thank Mr. Tim Schumacher for conducting the turning experiments and the force measurements.

7 REFERENCES

[Sun 2013] Sun, S. Brandt, M. and PT Mo, J. Evolution of tool wear and its effect on cutting forces during dry machining of Ti6Al4V alloy. Journal of Engineering Manufacture, 2014, Vol.2, pp 191-202.

[O'Sullivan 2001] O'Sullivan, D and Cotterell, M. Temperature measurement in single point turning. Journal of Materials Processing Technology, 2001, Vol.118, pp 301-308.

[Tönshoff 2000] Tönshoff, H.K., Arendt, C. and Ben Amor, R. Cutting of Hardened Steel. CIRP Annals, 2000, Vol.49, No.2., pp 547-566.

[Agapiou 2013] Agapiou, J. and Stephenson, D.A. Cutting Tool Wear and Failure Mechanisms. Encyclopedia of Tribology, Springer, Boston, MA, 2013, ISBN 9780387928975.

[Astakhov 2004] Astakhov, V.P. The assessment of cutting tool wear. International Journal of Machine Tools & Manufacture, 2004, Vol.44, pp 637-647.

[Liu 2016] Liu, Z.Y. et al. Energy consumption and process sustainability of hard milling with tool wear progression. Journal of Materials Processing Technology, 2016, Vol.229, pp 305-312.

[Meyer 2012] Meyer, R., Köhler, J. and Denkena, B. Influence of the tool corner radius on the tool wear and process forces during hard turning. International Journal of Advanced Manufacturing Technology, 2012, Vol.58, pp 933-940.

[Özel 2009] Özel; T. Finite element simulation of machining nickel-based alloy in the presence of tool flank wear. CIRP Conference on Modelling of Machining Operations, Donostia-San Sebastian, Spain, 2009.

[Munoz-Sanchez 2011] Munoz-Sanchez, A et al. Numerical analysis of tool wear effect in the machining induced residual stresses. Simulation Modelling Practice and Theory, 2011, Vol.19, No.2., pp 872-886.

[Ducobu 2015] Ducobu, F. et al. Finite element prediction of tool wear influence in Ti6Al4V machining. Procedia CIRP, 2015, Vol.31, pp 124-129.

[Equeter 2018] Equeter, L. et al. Estimation of the influence of tool wear on force signals: A finite element approach in AISI 1045 orthogonal cutting, AIP Publishing, 2018, Vol.1960(1).

[Aridhi 2022] Aridhi, A. et al. Comparison of the CEL and ALE approaches for the simulation oforthogonal cutting of 15-5PH and 42CrMo4 materials. Journal of Engineering Manufacture, Vol.237(II), pp 1726-1736.

[Ducobu 2017] Ducobu, F. et al. The CEL method as an alternative to the current modelling approaches for Ti6Al4V orthogonal cutting simulation. Procedia CIRP, 2017, Vol.58, pp 245-250.

[Meurer 2022] Meurer, M. et al. Numerical prediction of machining induced residual stresses when hard cutting AISI 4140. Procedia CIRP, 2022, Vol.108, pp 583-588.

[Clavier 2024] Clavier, F et al. Towards the numerical simulation of tool wear induced residual stress drift. Procedia CIRP, 2024, Vol.123, pp 404-409.

[Langenhorst 2019] Langenhorst, L., Cihan, M. and Sölter, J. A three dimensional calculation approach for the heat flux density distribution in face milling. Procedia CIRP, 2019, Vol.82, pp 8-13.

[Johnson 1985] Johnson, G.R. and Cook, W.H. Fracture characteristics of three metals subjected to various strains, strain rates, temperatures and pressures. Engineering fracture mechanics, 1985, Vol.21, No.1., pp 31-48.

[Buchkremer 2017] Buchkremer, S. Irreversible thermodynamics of nano-structural surface modifications in metal cutting. Aachen: Apprimus, 2017, ISBN 9782863595081.

[Hammelmüller 2015] Hammelmüller, F. and Zehetner, C. Increasing numerical efficiency in coupled eulerian-lagrangian metal forming simulations. International Conference on Computational Plasticity: Fundamentals and applications, Barcelona, Spain, 2015, pp 727-733.

[Meurer 2020] Meurer, M. et al. Cutting force based surface integrity soft-sensor when hard machining AISI 4140. Tm-Technisches Messen, 2020, Vol.87, No.11., pp 683-693.